

Equalization for High-Bitrate Acoustic Backscatter Communication in Metals

Peter Oppermann
Hamburg University of Technology
peter.oppermann@tuhh.de

Christian Renner
Hamburg University of Technology
christian.renner@tuhh.de

Abstract

Acoustic backscatter communication allows sensors in challenging environments to transmit data with negligible energy cost and is especially useful where electromagnetic waves are infeasible. In acoustic channels, strong inter-symbol interference (ISI) poses a major challenge, which is usually—in conventional communications—mitigated with equalization. Backscatter channels, however, are nonlinear, and standard equalization techniques are not directly applicable. Our work demonstrates that, by mapping the tag’s load to emerging steady-states, the nonlinear channel can be split into a map and a linear channel, enabling standard equalization techniques. Employing our custom reader and tag hardware design in the guided-wave (GW) metal channel, we demonstrate that data rates can be increased more than five-fold compared to no equalization with negligible additional cost. We compare different algorithms for equalization, timing recovery, and interpolation. Moreover, we investigate the time-variability of the GW channel under realistic scenarios, e.g., varying temperatures and physical stress, and present an effective countermeasure to adapt to the time variance.

1 Introduction

Backscatter communication enables a variety of novel applications for wireless sensor nodes. The negligible energy requirement of passive communication allows sensor nodes to operate with smaller—or even without—batteries and, therefore, significantly reduces the cost and size of devices. However, radio-frequency waves are not suitable in all scenarios. Hence, the concept of backscatter was recently extended beyond radio-frequency waves, e.g., to visible light [1], or acoustic waves [18]. In underwater applications, where electromagnetic waves are exponentially absorbed [16], acoustic backscatter has been explored in [2, 3], reaching distances of up to 10 m. Similarly, acous-

tic backscatter may also power and read-out smart implants deep in the human body [4, 5]. Furthermore, the absorption of electromagnetic waves by metals makes acoustic through-metal backscatter a hot topic for sensors in closed containers, such as fuel tanks, or structural health monitoring (SHM) [12, 15, 18, 19].

Acoustic waves propagate several orders of magnitude slower than RF, e.g., only several km s^{-1} in metals and in water compared to the speed of light at which electromagnetic waves propagate. Furthermore, many environments have strong multipath characteristics, e.g., guided-wave metal channels or underwater channels in ports. Therefore, inter-symbol interference (ISI) often strongly limits data rates, especially in acoustic backscatter. At the same time, higher data rates enable novel applications and reduce the required total energy for communication at the tag and reader by reducing the transmission time, in which both need to be active. Therefore, battery-less microsystems in metals, underwater, or in the human body are in eyesight.

Traditional communication systems employ equalizers to combat ISI by learning and removing the multipath characteristics of the channel. Unfortunately, backscatter channels are often nonlinear [17], which prohibits the direct application of established and computationally efficient symbol-by-symbol equalization techniques. Existing work about equalizers in backscatter communications linearized channels with knowledge of the transmitted constellation [6]. In certain channel types, however, the channel severely distorts constellations, requiring a different approach.

In this work, we focus on acoustic guided-wave (GW) metal channels, as found in plate-like structures such as pipelines, struts, and beams. GW channels are particularly challenging because they i) show low attenuation and strong reverberation, ii) only allow low bandwidths and, hence, efficient utilization of the available bandwidth is essential, and iii) require highly flexible tuning of the carrier frequency dependent on the specific channel for maximum signal-to-noise ratio (SNR). We aim to increase the potential data rates of acoustic backscatter techniques by mitigating ISI in this channel type because it is an enabler for sensors for SHM, e.g., embedded within metals or in closed containers. However, the major takeaways are not limited to GW channels but also apply to other types of backscatter channels and may enhance communication in other areas, e.g., biomedical implants and underwater monitoring. Our contributions are

- an analysis of the characteristics of the acoustic GW backscatter channel, including proof that the nonlinear channel is equivalent to a mapping followed by a linear channel,
- a custom reader and tag design to enable higher-order backscatter communication,
- in-depth analysis of the potential of digital communications algorithms, including DF and MMSE equalization, channel parameter tracking, timing recovery, and channel coding in acoustic backscatter, and
- an investigation of effects of temperature and mechanical stress on the GW metal channel, and a strategy to mitigate errors through the time-varying channel.

Section 2 reviews the principles of acoustic backscatter communication and equalization. In Section 3, we first investigate the characteristics and challenges of the GW metal channel and derive the nonlinear channel function. We then show that the model can be split into a nonlinear load transformation followed by a linear channel, leveraging the knowledge of steady-states. We then can directly equalize the linear equivalent model with well-known equalization techniques. Section 4 presents the design of a custom reader and tag pair that can perform higher-order modulation with highly tunable carrier frequency by analog demodulation with a homodyne IQ demodulator. We then present the implementation details of a packet-based communication scheme. We compare two common types of equalizers, MMSE and decision feedback (DF), in the equivalent channel. Furthermore, we extend the conventional LMS algorithm to adapt equalizer coefficients to time-varying channel parameters and constellation points, covering the nonlinear variations in the backscatter channel.

With the presented implementation, we perform real-world tests on several metal channels and demonstrate that we achieve more than five times higher data rates with an equalizer than without over a distance of up to 3m. The presented adaption techniques can reduce the errors introduced by channel variations more effective than conventional LMS adaption, especially in rapidly changing channels.

2 Background

We first clarify the principle behind acoustic backscatter communication in metals and introduce the notation of the signals used throughout this work. We then introduce the fundamentals of the two equalizer types we apply.

2.1 Acoustic Backscatter

The backscatter communication system consists of a reader and a tag. Both are equipped with a piezoelectric transducer attached to a medium, e. g., a structural element. The reader generates an ultrasonic carrier by applying a continuous sine wave to its transducer while observing the current flow through the transducer simultaneously. The ultrasonic carrier propagates through the medium, and the tag's transducer converts the acoustic signal back into an electric signal. An impedance mismatch between the transducer's input impedance and the tag's circuit causes partial reflection of the incoming wave. The tag changes the transducer's reflection coefficient by modifying its input impedance and,

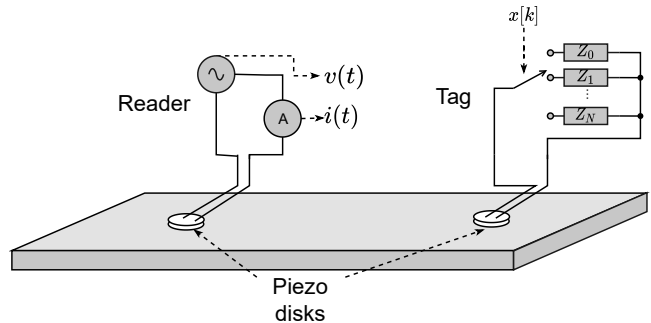


Figure 1. The principle of acoustic backscatter on a solid specimen (adapted from [18]).

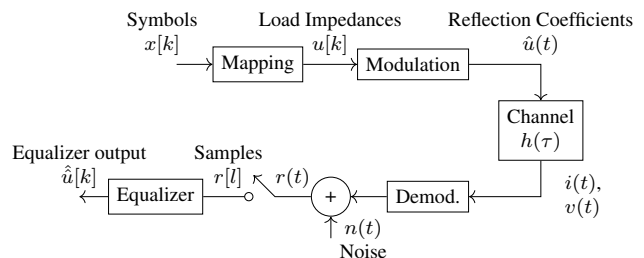


Figure 2. Block diagram of an acoustic backscatter communication system.

hence, modulates the reflected signal.

Figure 1 shows a schematic sketch of the physical setup of an acoustic backscatter system. We denote the sequence of transmitted symbols as $\mathbf{x} = [x_0, x_1, \dots, x_{K-1}]$, where each sequence element represents one out of N symbols, i. e., $\mathbf{x} \in \{0, 1, \dots, N-1\}^K$. The symbols map to a sequence $\mathbf{u} \in \{Z_0, Z_1, \dots, Z_{N-1}\}^K$ of load impedances at the tag. Finally, a load impedance causes the transducer to have a specific reflection coefficient, so the sequence of reflection coefficients is denoted as $\hat{\mathbf{u}} \in \mathbb{C}^K$. The reflection coefficients relate to the applied load impedance as

$$\hat{u}[k] = \frac{u[k] - Z_T}{u[k] + Z_T}, \quad (1)$$

where Z_T is the output impedance of the transducer.

The reader generates a continuous carrier $v(t)$ in the medium and simultaneously measures the current $i(t)$ through its transducer. Current and voltage are sinusoids at the carrier frequency. They are split up in the In-Phase and Quadrature components after demodulation, yielding a complex signal $r(t) = a(t) \exp(j \cdot \phi(t))$, where $a(t)$ is the current's amplitude, and $\phi(t)$ is the phase difference between current and voltage. After sampling at a constant rate T_s , this yields $\mathbf{r} = [r_0, r_1, \dots, r_{L-1}] \in \mathbb{C}^L$. Figure 2 shows the communication blocks to clarify further notation. We will use square brackets to refer to discrete-time signals and normal brackets to refer to continuous-time signals.

2.2 Equalization

Equalizers aim to remove ISI from a received signal. Sequence estimation with the maximum likelihood criterion is known to provide optimal performance but is too resource-

consuming for practical applications. Instead, symbol-by-symbol equalizers are typically used. Among these equalizers, linear equalizers and the decision feedback equalizer are popular because they can be implemented with simple digital filters. The filter coefficients can be learned efficiently from a pilot signal [7].

This work investigates the applicability of two types of equalizers to the acoustic backscatter channel: The linear minimum mean squared error (MMSE) equalizer, and the nonlinear decision feedback (DF) equalizer. Both types, however, build on the assumption of a linear channel, i.e., the received signal must be representable as a linear combination of the previously sent symbols.

$$r(t) = \int_0^\infty h(t - \tau)\hat{u}(\tau)d\tau, \quad (2)$$

where $\hat{u}(t)$ is the channel input and $h(t)$ is the channel impulse response. This assumption is, in general, not valid for the acoustic backscatter channel. We investigate the channel characteristics in more detail in Section 3.

The MMSE equalizer is a linear feedforward filter with N filter taps. It computes a linear combination of the last N samples, weighted with filter coefficients $c_i, i \in \{0, 1, \dots, N - 1\}$

$$\hat{u}_{\text{MMSE}}[k] = \sum_{i=0}^{N-1} c_i r[k - i]. \quad (3)$$

The name MMSE refers to the criterion of how the filter coefficients are computed. With a known training sequence \mathbf{u} , the MMSE equalizer optimizes the coefficients \mathbf{c} so that the error $\|\hat{\mathbf{u}} - \mathbf{u}\|$ is minimized in the sense of the minimum mean square criterion.

The DF equalizer, in contrast, uses a feedforward filter with the last P samples, and a feedback filter, using the last Q symbol decisions as feedback.

$$\hat{u}_{\text{DF}}[k] = \sum_{i=0}^{P-1} c_{f,i} r[k - i] - \sum_{j=1}^Q c_{b,j} \hat{u}[k - j], \quad (4)$$

where \mathbf{c}_f are feedforward filter coefficients and \mathbf{c}_b are the feedback filter coefficients.

2.3 Equalizer Comparison

The advantage of the DF equalizer is that it uses the hard decision of the previous symbols in the feedback loop for ISI removal instead of noisy past samples. Therefore, the MMSE equalizer output is noisier than the DF equalizer. A disadvantage of the DF equalizer is error propagation, i.e., when a wrong decision was made about a symbol, this error affects the following symbols.

Another difference is the required number of taps. In many practical applications, the signal is oversampled with a multiple L of the symbol rate f_M . The number of taps must be large enough to span the delay spread σ of the channel. Hence, when the delay spread spans M symbols, the required number of taps in a fractionally spaced MMSE equalizer is $N = M \cdot L$. At the same time, the DF equalizer only uses the past symbol decisions in its feedback loop and hence only

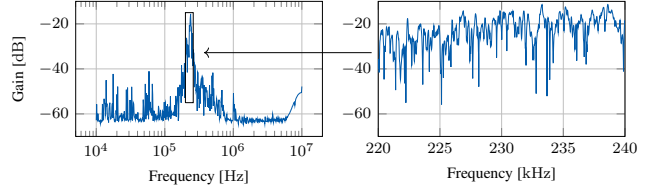


Figure 3. Gain of a guided-wave metal channel, where the output voltage was measured at the tag’s transducer 3 m away from the reader on a steel plate.

uses $Q = M$ taps in the feedback and $P = L$ taps in the feed-forward filter. Therefore, the DF equalizer is less computationally intense and can converge on shorter pilot sequences, as we investigate in Section 5.1.

3 Acoustic Backscatter Channel

We investigate the characteristics of GW metal channels and demonstrate that conventional techniques from backscatter communication need to be adapted to work in this environment because signal constellations are generally unknown to the reader. We then introduce a model for the multipath backscatter channel and demonstrate our novel approach to splitting the nonlinear channel into a mapping followed by a linear channel without relying on knowledge of the constellation.

3.1 Channel Characteristics

In a GW metal channel, the transducers are applied to a plate-like structure as shown in Fig. 1. The type of wave propagating with the lowest attenuation over such a structure is the so-called lamb wave. It can only be excited efficiently in frequency ranges, where the wavelength is in the order of magnitude of the plate thickness [8]. Accordingly, existing work on active acoustic guided-wave metal communication employed frequencies between 20 kHz and 400 kHz [9, 10], strongly limiting the available bandwidth.

Figure 3 (left) shows the one-way channel frequency response in a 5 mm test plate, where reader and tag are 3 m separated. Note that the backscatter signal must propagate two-way, doubling the attenuation in dB. The figure (left) shows that—in this specific channel—we can only utilize a narrow frequency band around 220 kHz. The structure’s thickness and material determine the broad utilizable bandwidth in which lamb waves can be excited efficiently. Furthermore, piezo disks have a narrowband characteristic, additionally limiting the bandwidth. Attempts to develop broadband transducers exist but require complex and expensive transducer designs [13]. Figure 3 (right) shows an excerpt of the frequency response in the usable band, demonstrating that the channel is strongly frequency selective, mainly caused by the multipath characteristics of the structure at hand. This frequency selectivity motivates that a backscatter reader must adapt the carrier frequency to the channel and can not rely on a fixed carrier.

Previous work on higher-order modulation in backscatter communication chose the load impedances at the tag based on the input impedance of the antenna, or transducer, respectively [3, 22]. We can choose the optimal load impedances to achieve the desired constellation using Eq. (1). In the

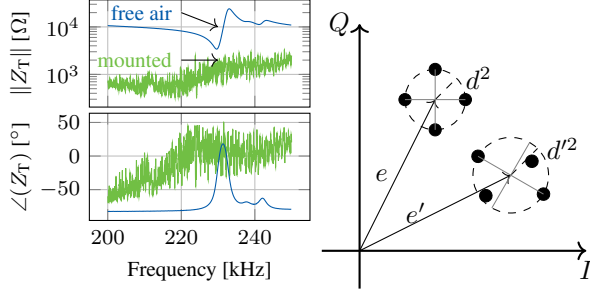


Figure 4. Input impedance of the tag’s piezo when mounted on a metal plate compared to free air (left). When using the same load impedances at the tag with two different channels, the resulting constellation is distorted nonlinearly (right).

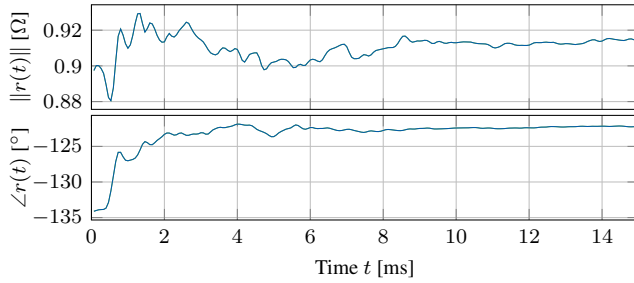


Figure 5. Observed step response in a GW metal channel under test.

GW metal channel, however, the coupling between transducer and metal is so strong that the channel heavily distorts the transducer’s input impedance. Figure 4 (left) shows the measured input impedance of the same transducer, once in free air and mounted on a metal plate. The impedance in free air follows a smooth, typical curve. After mounting it on the structure, the transducer’s input impedance fluctuates strongly, changing between capacitive and inductive within a few hertz. The strong electromechanical coupling between piezoelectric transducer and metal structure [21] is the cause for this effect. Therefore, it is infeasible to match the transducer’s impedance at the tag without prior channel measurement, which is impractical and would require custom adaptation of the tag hardware for every individual placement. Our approach assumes that we do not know the input impedance and that the resulting constellation is unknown to the reader.

Lastly, Fig. 5 shows an investigation of the step response at the reader when the tag switches between two load states. We observe that significant inter-symbol interference exists on the channel, and it takes roughly 8 ms to 10 ms until the received signal converges to a new steady-state in this specific channel. An equalizer is required to reduce ISI and allow symbol times much smaller than this.

3.2 Channel Model

We present a model of the backscatter channel to emphasize its nonlinear characteristics. We then show that an equivalent linear channel exists that we can instead use for equalization. This equivalent channel is based on the *steady-state* for each symbol at the tag. A channel is linear when

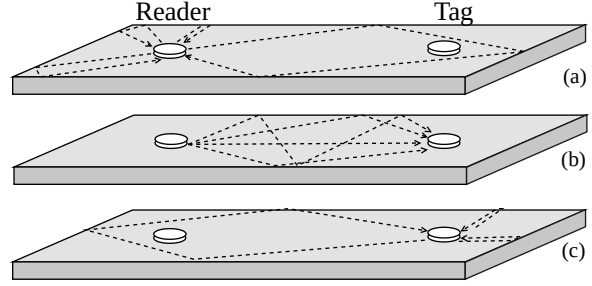


Figure 6. Visualization of the paths in the structure, where (a) shows the static environment paths, (b) shows the paths from the reader to the tag, and (c) shows higher-order scattering.

a linear relationship between input and output exists, which raises the question of what we should consider as channel input. The chosen load impedance $u[k]$ at the tag has a highly nonlinear relation with the resulting reflection coefficient (see Eq. (1)), and, as we demonstrated, this relation is unknown a priori. We will therefore continue to use the reflection coefficient in the model as channel input.

We assume the backscatter channel to be a multipath channel. The carrier originates at the reader and propagates through the structure over multiple paths. The received signal is then again captured by the reader. Every propagation path is characterized by three properties: an attenuation factor a , a phase shift ϕ , and a propagation delay τ . A subset of paths \mathcal{P}_E are reflections of the carrier from the environment, i. e., the structure’s boundaries. These paths are static and not influenced by the transmitted symbol. Another subset of paths, \mathcal{P}_D , describes the dynamic paths, the paths that lead from the reader to the tag’s transducer. The same set \mathcal{P}_D also leads from the tag to the reader in the other direction. The two types of paths are visualized in Fig. 6 (a) and (b).

The constant carrier in baseband is denoted as a complex factor $c = A_0 \cdot e^{j\phi_0}$, and the tag’s time-varying reflection coefficient is $\hat{u}(t)$. Then the received signal can be described as

$$r(t) = c \cdot \left[e + d \sum_{r \in \mathcal{P}_D} a_r \cdot \exp(j\phi_r) \hat{u}(t - \tau_r) + \vartheta \right], \text{ with} \quad (5)$$

$$e = \sum_{p \in \mathcal{P}_E} a_p \cdot \exp(j\phi_p) \quad (\text{Environment})$$

$$d = \sum_{q \in \mathcal{P}_D} a_q \cdot \exp(j\phi_q) \quad (\text{Carrier at tag}),$$

where e is the sum of all reflections from the environment and d is the carrier that is observed at the tag’s transducer. Note, that both e , and d are not time-dependent, as the reader applies a constant carrier, and after few milliseconds, a steady-state emerges as paths with a longer transmission time have been attenuated under the noise threshold. The time-dependent part is the reflection from the tag, with a time-varying reflection coefficient.

In our model, we only treated direct reflections. On some paths, a signal is reflected by the tag’s transducer multiple

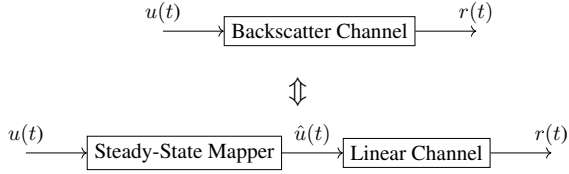


Figure 7. The nonlinear baseband backscatter channel can be equivalently represented by a mapping from load impedances to steady-state values followed by a fully linear communication channel.

times before returning to the reader. Such paths introduce the residual ϑ , where the reflection coefficient is applied multiple times. Since these multi-reflections have to travel longer distances and experience more reflections from the metal boundaries, they are usually small in magnitude, and we will neglect them, i.e., $\vartheta \approx 0$.

Equation (5) shows that the received signal consists of a constant offset e , and the reflected signal may be scaled and rotated in the I-Q plane by the propagation path d , as depicted in Fig. 4 (right). Due to the offset, the received signal is not linearly dependent on the scattered signal. Conventional backscatter systems removed the offset e from the signal, e.g., by removing the mean of the received signal, successfully linearizing the channel. This, however, requires a symmetric constellation, where e equals the mean of all constellation points. Since—in GW channels—the constellation is unknown and is likely not symmetric, the offset can not be removed, and the received signal can not be linearized.

However, we can change what we consider the channel input to yield a linear relationship between channel input and output. Consider the steady-state value \tilde{u}_i , which is the value that the received signal converges to when the tag applies a constant load impedance for a sufficiently long time. In that case, $\hat{u}(t)$ is independent of the path delay τ for all paths in \mathcal{P}_D , yielding

$$\begin{aligned} \tilde{u}(t) &= c \cdot \left[e + d \cdot \hat{u}(t) \cdot \sum_{r \in \mathcal{P}_D} a_r \cdot \exp(j\phi_r) \right] \\ &= c \left(e + d^2 \hat{u}(t) \right). \end{aligned} \quad (6)$$

Solving this for the reflection coefficient gives

$$\hat{u}(t) = \frac{\tilde{u}(t)/c - e}{d^2}. \quad (7)$$

Plugging Eq. (7) into Eq. (5) produces

$$\begin{aligned} r(t) &= c \left(e + d \sum_{r \in \mathcal{P}_D} a_r \cdot \exp(j\phi_r) \frac{\tilde{u}(t - \tau_r)/c - e}{d^2} \right) \\ &= c \left(e + \frac{1}{d} \sum_{r \in \mathcal{P}_D} a_r \cdot \exp(j\phi_r) \frac{\tilde{u}(t - \tau_r)}{c} \right. \\ &\quad \left. - \frac{e}{d} \sum_{r \in \mathcal{P}_D} a_r \cdot \exp(j\phi_r) \right) \\ &= \frac{1}{d} \sum_{r \in \mathcal{P}_D} a_r \cdot \exp(j\phi_r) \cdot \tilde{u}(t - \tau_r). \end{aligned} \quad (8)$$

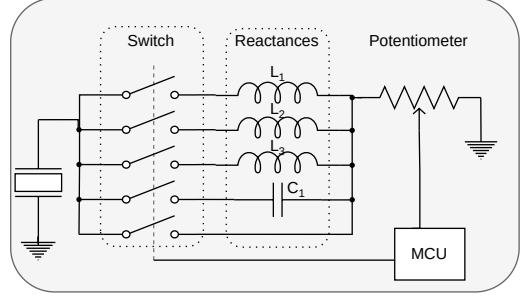


Figure 8. Tag schematic overview. A microcontroller (MCU) controls a set of switches and a potentiometer to vary the transducer’s load impedance (adapted from [18]).

Equation (8) shows that the relation between steady-state values and channel output is linear. That means a backscatter channel behaves equivalent to a conventional linear channel following mapping from load impedances to emerging steady-state values (see Fig. 7). As the reader had no option to know the reflection coefficients a priori, it can easily acquire the steady-state values from a pilot sequence in a channel estimation step. Hence, the reader can acquire the required information to train and apply an equalizer to the received signal.

4 Implementation

This section first motivates and explains the chosen implementation of the reader and then focuses on the software pipeline that the reader employs to decode the messages.

4.1 Hardware

We present a custom hardware design for reader and tag because a) no commercially available integrated circuits (ICs) suitable for acoustic backscatter exist on the market, and b) we want to demonstrate that reader and tag can be constructed from cheap, commercial off-the-shelf (COTS) components. Available readers for RF backscatter are designed for frequency ranges of several hundred MHz to a few GHz, while the most effective acoustic waves in guided-wave metal channels are in much lower ranges of a few hundred kHz. In underwater environments, they even go as low as tens of kHz [2]. Most existing designs for acoustic through-metal backscatter communication in SWP channels employed binary modulation with only ASK modulation. For higher-order modulation, however, quadrature modulation is desired. Our tag and reader are a modification of our previously presented hardware [18]. We extended the reader with an analog demodulator circuit, allowing a higher frequency resolution than with digital demodulation.

The tag must switch between a set of load impedances applied to its transducer (Fig. 8). As we demonstrated, we cannot know the best load impedances for a channel a priori. The tag must be able to choose flexibly between different load impedances. Therefore, our design can vary both its load’s reactance and resistance. It employs a set of inductors and capacitors that can be selected dynamically and a digital potentiometer in series with the reactances. From the preliminary measurements shown in Fig. 4, we pick optimal

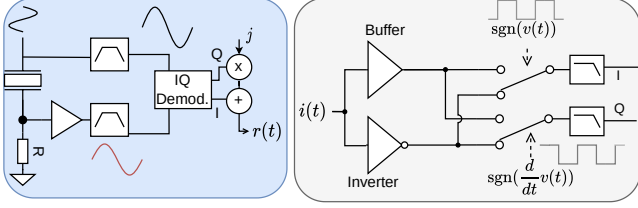


Figure 9. Principle sketch of analog IQ demodulator. Inverter, buffer, and derivative are realized with operational amplifiers, while the sign operation is realized with a comparator.

loads for the average input impedance between 220 kHz to 230 kHz. The switch and potentiometer are digitally controlled with a microcontroller.

The reader’s job is to i) generate a sinusoidal carrier wave with a finely tunable frequency and ii) to measure the current through the transducer and decompose it into an in-phase and a quadrature component relative to the voltage applied to the transducer. In contrast to many conventional communication schemes, we dynamically adapt the carrier frequency to the channel because the SNR can be improved significantly by using a resonant frequency for a specific channel. Furthermore, the reader and tag are not mobile, so the channel—and the optimal carrier frequency—is not expected to present strong time-variance. The carrier is generated with a direct-digital-synthesis IC (AD9833), with which the STM32F446RE microcontroller can tune the frequency with an accuracy of less than 20 mHz.

Although it is possible to use digital IQ demodulation to recover the phase and magnitude of the received signal with lower carrier frequencies, we decided to implement an analog demodulator because

- fast digital demodulation techniques require certain relations between sampling frequency and carrier frequency, limiting the resolution of achievable carrier frequencies significantly,
- no additional local oscillator is required because the reader both generates the carrier and demodulates the received signal in a single device,
- analog demodulation allows the MCU to sample the signal at rates much lower than the carrier frequency, reducing the load on the MCU.

Again, no COTS ICs for IQ demodulation or frequency mixing were available because of the unusually low frequency range. Therefore, we constructed a mixer from analog switches (Fig. 9). The lowpass filters are third-order Butterworth filters with a cutoff frequency of 10 kHz. Lowpass filtering is required to remove the frequency components at multiples of the carrier frequency that arise during mixing. The result is a DC signal where

$$I(t) \propto \|i(t)\| \cdot \cos \angle \{i(t), v(t)\} \quad (9)$$

$$Q(t) \propto \|i(t)\| \cdot \sin \angle \{i(t), v(t)\}. \quad (10)$$

4.2 Message Structure and Sending

After establishing signals’ physical generation and reception, we explain the package-based message structure for communication. We prepend every message with a preamble, a 13 symbol barker sequence with optimal correlation properties. Following the preamble, we transmit the encoded symbols. During transmission, the tag switches to a unique load impedance for every transmit symbol with a given symbol frequency $1/T_m$.

As we aim to explore the limitations of the backscatter channel, we also applied strong channel coding. As a code, we chose LDPC codes, which can be encoded with little computational effort at the resource-constrained tag. Performance depends strongly on the properties of the specific channel code. Therefore we decided to adopt a standardized code from WiMAX, retrieved from [11]. The code has a block length of $N_b = 576$ information bits, and a code rate of 0.83, yielding 478 information bits per message. The number of symbols in a message also depends on the modulation order and is denoted as $N_s = \lceil N_b = \log_2(N) \rceil$ symbols.

4.3 Software-Defined Radio Pipeline

After analog demodulation, the in-phase and quadrature parts are sampled simultaneously with the 12-bit ADC integrated into the MCU. We used a sampling rate of 100 kHz and then passed the acquired samples through a digital 4-th order lowpass filter. Filtering is required because, after the analog demodulation, we still observe noticeable leakage of the carrier frequency in the received samples. Furthermore, the digital filter can easily be tuned to the required bandwidth, which varies with symbol time. Accurate tuning of the cutoff frequency is essential because the transmitted signal is not bandlimited, i.e., the tag can not apply a pulse shaping filter. By switching between loads, the scattered signal effectively has a rectangular pulse shape with infinite bandwidth. Adapting the lowpass filter accordingly will prevent severe aliasing.

We then downsample the filtered signal to a multiple L of the symbol rate. In our experiments, we have used values for L between 4 and 10 because at least four samples per symbol are required for the following symbol timing detection. Finally, the I and Q part are combined to form a complex number, i.e.,

$$r[l] = I(l \cdot T_s) + j \cdot Q(l \cdot T_s). \quad (11)$$

We perform channel activity detection, symbol timing synchronization, channel equalization, and frame synchronization for successful message reception. In the following steps, we assume that the reader already has the required channel state information, i.e., the steady-state channel values corresponding to every symbol and the equalizer coefficients. We will focus on the channel estimation step in Section 4.4.

Activity detection aims to detect the start of a message coarsely. Therefore, incoming samples are written to a buffer. For every block of N_A samples, a standard deviation is calculated. If this does not exceed a fixed threshold, we discard the block. Otherwise, the receiver passes the samples through symbol timing detection, where we use a square timing error detector to identify the sample timing offset. We subsequently interpolate samples to reconstruct

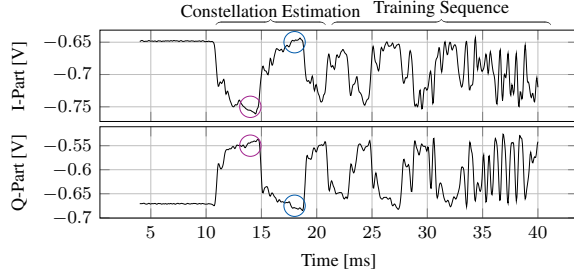


Figure 10. A training sequence for the equalizer. The constellation points are estimated at the start of the sequence, where the same symbols are sent multiple times consecutively to let a steady-state emerge.

the samples at the correct sampling instants with either a linear or a square interpolator. We compare the effectiveness of different interpolators in Section 5.

Next, the samples are equalized either with the linear MMSE equalizer or with a DF equalizer. After that, we use a correlation to find the preamble, and the resulting samples are either fed into a decoder for the channel code or passed through a hard decision device to yield the final message.

4.4 Equalizer Training and Adaption

The reader must acquire channel state information for equalization, i.e., the equalizer weights. The tag sends a known training sequence beforehand. Knowing the sent and received signal, the channel can be estimated with linear least-squares optimization. However, in contrast to conventional communication systems, where constellation points are known to sender and receiver beforehand, the constellation points in the equivalent linear channel depend on the nonlinear backscatter channel, and the reader can not know them a priori. Therefore, the reader needs to acquire knowledge about the constellation points additionally.

Therefore, the tag's training sequence starts with a sequence, where every symbol is repeated for multiple symbol periods (see Fig. 10). When the symbols are repeated long enough, the steady-state will emerge. In the channels evaluated by us, ten milliseconds are sufficient. From these sequences, the reader can then extract knowledge about the mapping from symbols to constellation points. With this, it can also reconstruct the input to the equivalent linear channel that is required for equalizer training.

Equalizer Tracking

Although reader and tag are not mobile, the channel may change over time due to temperature changes in the structure or altered boundary conditions. We leverage adaptive equalization to adapt the equalizer weights to the varying channel continuously. Therefore, we implement the LMS algorithm, where the equalizer error is estimated after equalizing every symbol, and the equalizer parameters are adapted to reduce the observed error.

However, in contrast to conventional communication, the constellation points may also change when the channel varies. When the estimated constellation points are not representing the steady-state values correctly, the assumed

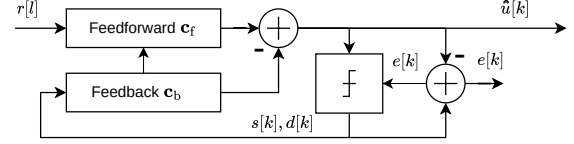


Figure 11. Schematic of a decision feedback equalizer with error term. The decision device outputs the detected constellation point $d[k]$, and the symbol index $s[k]$ corresponding to this constellation point.

equivalent channel is not truly linear. Therefore, the equalizer performance will degrade. For proper tracking of the channel parameters, we also require an adaptive tracking of the constellation points.

The core idea is to split the parameter update into two steps. In the first step, we assume the estimated constellation points are correct and update the equalizer taps according to the regular LMS algorithm. In the second step, we assume that the equalizer taps represent the channel perfectly so that the mean value of every equalized symbol is distributed around the corresponding correlation point with zero mean. Therefore, during the second step, we slightly adapt the constellation point of the currently detected symbol in the direction of the error.

We illustrate this technique using the decision feedback equalizer shown in Fig. 11, although it can also be used with an MMSE equalizer analogously. The decision device uses the i -th estimate of the constellation points z_s^i corresponding to the symbol s . After every detected symbol, the detector updates its constellation point estimation opposite the equalizer error's direction. At the same time, the equalizer coefficients \mathbf{c}_f and \mathbf{c}_b are updated as in the LMS algorithm.

$$\begin{aligned}
 e[k] &\leftarrow d[k] - \hat{u}[k] \\
 \mathbf{c}_f &\leftarrow \mathbf{c}_f + 2\mu_c \cdot e[k] \cdot \bar{r}[k, \dots, k-P] \\
 \mathbf{c}_b &\leftarrow \mathbf{c}_b - 2\mu_c \cdot e[k] \cdot \bar{d}[k, \dots, k-Q] \\
 z_{s[k]} &\leftarrow z_{s[k]} - \mu_z e[k],
 \end{aligned}$$

where \bar{r} is the complex conjugate of the received samples, and \bar{d} is the complex conjugate of the previous symbol decisions. Both adaptations are scaled with a factor μ_c , or μ_z , respectively, to avoid instability. The effectiveness of the constellation point adaption is evaluated in section Section 5.5.

5 Evaluation

We first evaluate the influence of tap number and training sequence length for both equalizer types, DF and MMSE. We then focus on the sampling timing mismatch and interpolation techniques. Then, we investigate the gain of channel coding. Next, we compare the total achievable data rate with and without the applied equalization techniques. Then, we explore the time-variance of the channel and the effectiveness of the proposed adaption technique. Finally, we study the linearity of the developed IQ demodulator.

We use a long metal bar with multiple transducers attached (see Fig. 12) for testing. The piezoelectric disks from PICeramics have a thickness of 2 mm and a diameter of 1 cm.

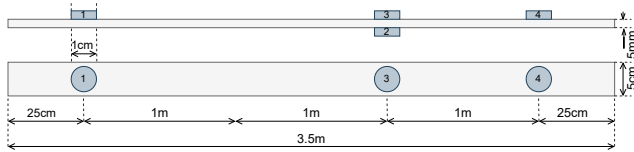


Figure 12. The specimen under test has a total length of 3.5 m and multiple piezos allow for several channels with different total lengths (not to scale).

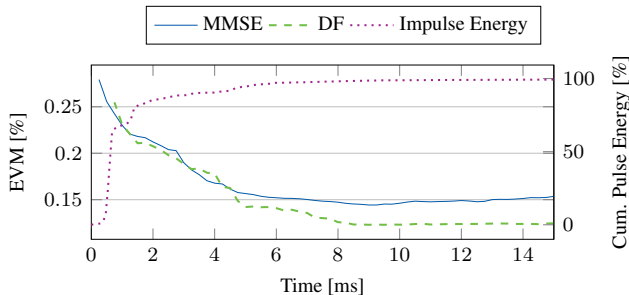


Figure 13. The chosen number of taps of the equalizer directly translates to the time span it can cover. Too many taps are degrading performance by overfitting.

The manufacturer specifies the resonant frequency in radial direction as 200 kHz, and in thickness mode as 1 MHz.

5.1 Equalizer Parameters

An established metric for evaluating equalizer performance is the error vector magnitude (EVM) [14, 22]. This is defined as the average RMS distance between the equalizer output and the correct constellation points relative to the average distance between constellation points.

$$\text{EVM} = \sqrt{\frac{1/K \sum_{i=0}^{K-1} \|\hat{a}[i] - u[i]\|^2}{1/N_s \sum_{i,j,i \neq j} \|Z_i - Z_j\|^2}} \quad (12)$$

We first evaluate the equalizer's required length, which directly translates to the timespan in which ISI can be removed. In our specimen channel, 9 ms was the optimal timespan for the equalizer. In direct comparison, the DF equalizer performed better than the MMSE equalizer. This is shown in Fig. 13, where we took a recording of 50 messages in a 1m channel with a symbol duration of 0.25 ms and an oversampling rate of 5. Regardless of the number of taps, we trained the equalizer with the same pilot message. The DF equalizer reached a minimum EVM of 12.3 % compared to 14.4 % for the MMSE equalizer. As a reference, we also show the cumulative energy of the impulse response in the same channel. The 9 ms optimum equalizer length span close to 100 % of the impulse response's energy.

Next, we investigate the relation between the length of the pilot sequence for equalizer training and the EVM in subsequent decoding. We used the same set of recorded messages but cropped the training sequence to a limited number of training symbols. We then equalized all 50 messages and compared the average EVM. The results show that the MMSE equalizer requires a longer training sequence than the

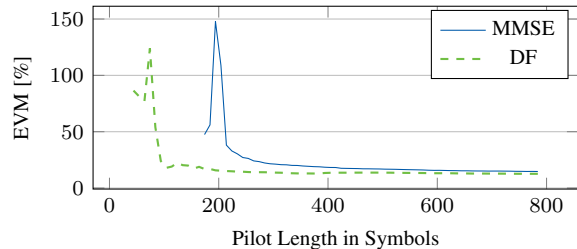


Figure 14. The DF equalizer requires significantly less taps and hence a shorter pilot sequence is sufficient for equalizer training.

DF equalizer, which can be explained by the much smaller number of filter coefficients required by DF. In this example, a pilot sequence of 100 symbols for the DF equalizer produces an EVM of 18 %, while the MMSE equalizer requires at least 400 symbols to generate the same EVM. An optimum is reached for the DF equalizer after 350 symbols, as shown in Fig. 14.

5.2 Sampling Timing Mismatch

When the analog signal is sampled at a fixed rate, an arbitrary delay τ is introduced because of the lack of synchronization between reader and tag, i. e., the sampled signal is

$$r[l] = r(l \cdot T_s + \tau(t)) \quad (13)$$

with sampling period T_s . When the pilot signal is received with delay τ_0 , the equalizer is trained to remove the ISI at sampling points with this specific delay. Upon reception of consecutive messages with $\tau \neq \tau_0$, the equalization performance is reduced.

We implemented a square timing error detector and interpolated the received samples according to the detected timing offset to mitigate the effects of timing errors. Evaluation in a real channel shows that timing error correction strongly reduces the EVM variability over a number of consecutive messages with arbitrary sampling delay. We also tested hard synchronization as a reference for optimal timing, where we used a cable to trigger the reader's sampling clock upon the start of transmission by the tag. Figure 15 (left) shows the error for 50 messages. It can be seen that without timing recovery, the equalizer error varied significantly between messages. The variation was strongly reduced with a square timing error detector and subsequent interpolation. However, hard synchronization still performs slightly better.

We want to note that, generally, τ can vary within one message due to clock frequency mismatch between tag and reader. Our implementation detected and corrected the timing mismatch for the whole message. Other timing error detector algorithms exist, capable of continuously adapting the timing error correction from one symbol to the next. These may still improve the results. However, we do not think that clock mismatch poses a large problem, as the clocks on the microcontrollers of reader and tag have a specified error of less than 1 %. Hence, during the 200 ms to 400 ms long messages, the total clock error should not exceed 0.2 % to 0.4 % of a sampling interval, depending on message length. In contrast, the initial offset τ at the start of a message can be up to

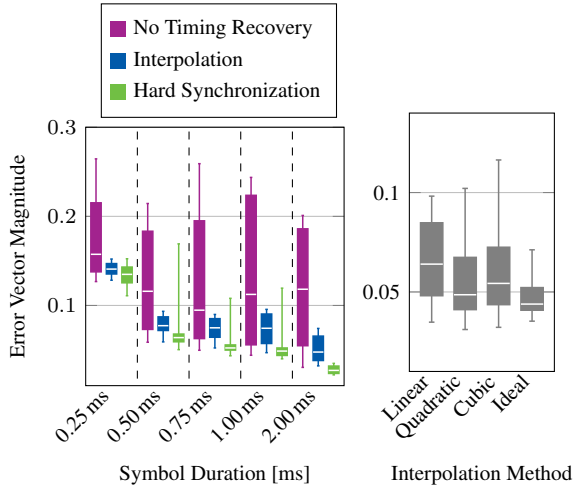


Figure 15. Influence of synchronization mismatch on equalizer output error EVM in a 2 meter channel for 50 messages each. The box shows the EVM range within which 90 % of the equalized messages fall, while the white line shows the median. Timing recovery successfully reduces variations in output error between messages, although it can not reach the optimum (hard synchronization).

half of a sampling interval and is much more relevant than clock drift.

We further investigated different methods for interpolation, i.e., linear, quadratic, cubic, and ideal interpolation. The ideal case involves a fast Fourier-transformation (FFT), multiplication in frequency domain, and inverse FFT, and is, therefore, very resource-consuming. We, therefore, consider it not as a viable solution for the reader, but as a reference for the optimal interpolation. Differences in overall performance between the different interpolations are minor, as shown in Fig. 15 (right). As expected, the ideal interpolation performs best. A quadratic interpolation scheme offers the best trade-off between implementation complexity and EVM.

5.3 Channel Coding

Channel coding and equalization must be considered jointly when designing a communication system. According to the literature, the DF equalizer has the disadvantage of error propagation, and that successive channel decoding can not improve on the propagated errors [7, p. 364f]. However, our results indicate that the decision feedback equalizer still outperforms the MMSE equalizer even after channel coding. Furthermore, we observe that channel coding improves the error of a DF equalizer.

Figure 16 compared the DF and MMSE equalizers with and without channel coding. We have again taken a recording of 50 messages in channel GW1, where the bits were encoded with a high rate ($R=0.83$) LDPC code from [11]. On the receiver side, the messages are decoded with an iterative belief propagation decoder with a maximum of 10 iterations. As a reference, we perform a hard decision on the information bits before decoding. To inspect the effect of lower SNR on the same channel, we add normal-distributed noise to the

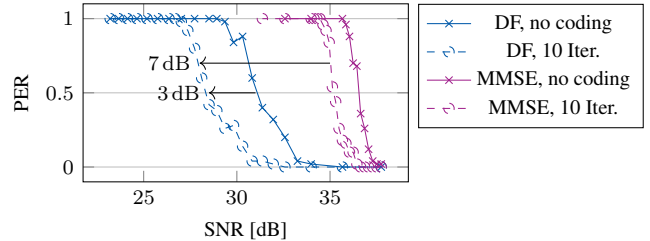


Figure 16. The packet error rate (PER) of the equalized channel with and without decoding. Iterative belief propagation decoding was performed with a maximum of 10 iterations. Here, a symbol interval of $T_m = 0.25$ ms, and 4-QAM like modulation was used.

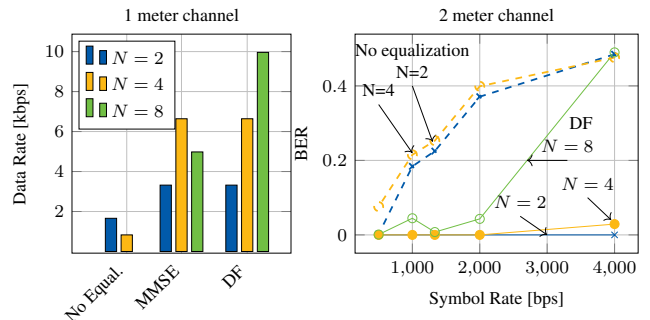


Figure 17. Achievable error-free throughput with the different configurations. The results were achieved on channel GW1 with channel coding.

recorded samples before equalization and decoding.

The results show a larger coding gain for the DF equalizer than for the MMSE equalizer (3 dB vs 1 dB), and a considerable gain of 7 dB between DF and MMSE equalizer regardless of coding. That indicates that the decision feedback equalizer is the better choice also after decoding.

5.4 Achievable Data Rate

We compare the increase in data rate over the metal channel achievable through equalization. The reference without equalization is established by picking the sample in the center of each symbol period and using it directly as input to the decoder. We recorded 100 messages for symbol durations $T_m \in \{0.25$ ms, 0.5 ms, 0.75 ms, 1 ms, 2 ms $\}$, and $N = \{2, 4, 8\}$ distinct constellation points. The results show that without equalization, the highest data rate is less than 2 kbit s $^{-1}$ in the 1m channel, and higher-order modulation with eight constellation points can not be achieved at all. The MMSE equalizer already triples the achievable data rate, and the DF equalizer even reaches more than five times the data rate, establishing error-free communication with eight constellation points per symbol at 4000 symbols per second. In the 2 m and 3 m channel, similar results are achieved. However, the data rates all overall reduced with maximum 6.6 kbit s $^{-1}$ with a DF equalizer and only 830 bit s $^{-1}$ without equalization, as shown in Figure 17. In all configurations, we equally applied timing recovery and channel coding.

To put this into perspective, we also calculated the Shan-

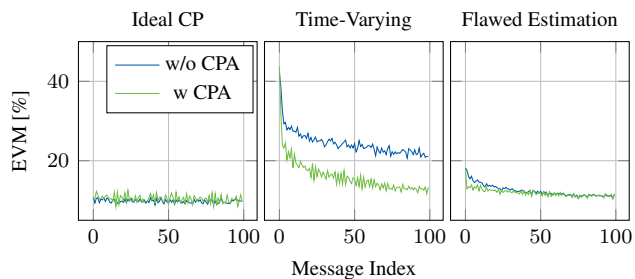


Figure 18. Error with and without constellation point adaption (CPA) in different scenarios.

non capacity limit of the channel using the impulse response and the water filling power allocation as described in [7, p116ff]. In channel GW1, the capacity was 66 kbits^{-1} , which is roughly 6.6 times larger than the maximum data rate achieved. The reason for this still large remaining gap is not apparent. However, reasons can be i) the short block length, as strong channel codes are known to reach the capacity limit only if block lengths approach infinity, and ii) nonlinearities in the receiver and the channel, as equalization and decoding algorithms are designed for a linear channel.

5.5 Time Variance and Adaption

We introduced our constellation point adaption (CPA) technique in Section 4.4. We now investigate the errors introduced by changing channel values and the effectiveness of the presented countermeasures.

As we cannot change the channel in a controlled way, we introduce an error to the estimate of the constellation points on purpose to evaluate how the CPA mechanism improves the result compared to conventional LMS. A recording of 100 sequential messages in a time-invariant channel is used, in which we know the correct constellation points from a channel estimation step. We distinguish three different scenarios:

1. *Ideal CP estimation*: The equalizer knows the correct constellation points during training and message reception.
2. *Time variant channel*: The equalizer can extract the correct constellation points from the training symbol and uses them for training. After training, the channel changes, and the constellation points are not correct anymore during message reception.
3. *Flawed channel estimation*: The estimated constellation points are not correct during training and reception.

In the latter two scenarios, we mimic a variation in the channel or an inaccurate channel estimation by adding an offset to the correct constellation points that we provide to the equalizer.

The results are shown in Fig. 18. In the ideal scenario, CPA produces roughly the same error as conventional LMS, but there is stronger variation in the performance between messages since noise in the recorded signal will cause non-beneficial adaptations to the constellation estimation. In the time-varying scenario, where the equalizer is trained with the

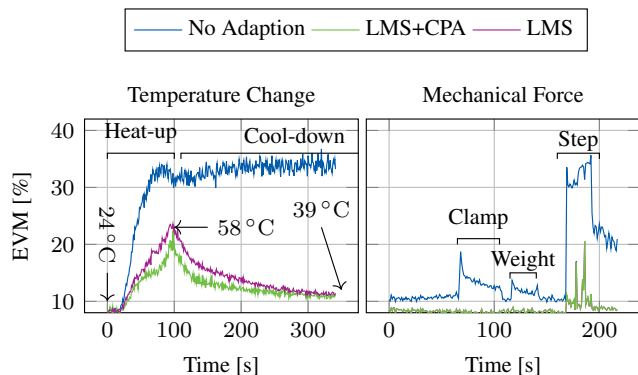


Figure 19. With static equalizer coefficients, the EVM rises strongly upon temperature variations in the material. Adaptive equalization using LMS and CPA can reduce the EVM and mitigate communication failure due to channel variation.

correct constellation points, CPA strongly reduces the EVM from initially 40 % to less than 13 %, close to the ideal values of 10 %. At the same time, without CPA, the LMS algorithm can adapt the channel parameters to reduce the error from 42 % to 21 %.

Finally, in the last scenario, where we already performed training on an inaccurate estimate of the constellation, both LMS alone and LMS with CPA can slightly improve EVM. However, the CPA algorithm does so much quicker within the first messages. These results show that the correct estimation of the constellation points from the training symbol is crucial for good equalization performance in any case. However, CPA can be used to track time-varying constellation points. CPA will, however, slightly degrade EVM in the ideal case when no variation in the channel exists.

In the second experiment, we apply CPA in two real-world scenarios: In the first scenario, temperature variations in the metal cause the channel to change, while in the second scenario, we expose the specimen to external forces. We first performed channel estimation with equalizer training in both scenarios and then continuously sent messages over a 1-meter channel for several minutes. We then evaluated the same recorded samples without adaption, with LMS adaption only, and with LMS and CPA. The setup with all used equipment is depicted in Fig. 20.

Figure 19 (left) shows the average EVM per message over time, while we heated the metal bar with a hot air gun from initially 24°C to up to 58°C . In outdoor environments, such temperature spans are feasible, though usually, temperature changes more gradually over the day. The heating and temperature measurement was performed locally between the two transducers. Without adaption, the EVM quickly rises as we begin to heat up the metal. After about 35 s, the equalizer output is so distorted that subsequent correlation fails to detect a message. LMS improves the EVM and enables continuous reception during the entire experiment. Finally, with CPA, all messages were also successfully received. The EVM with CPA was lower than with LMS only over the whole course of the experiment. However, we observed im-

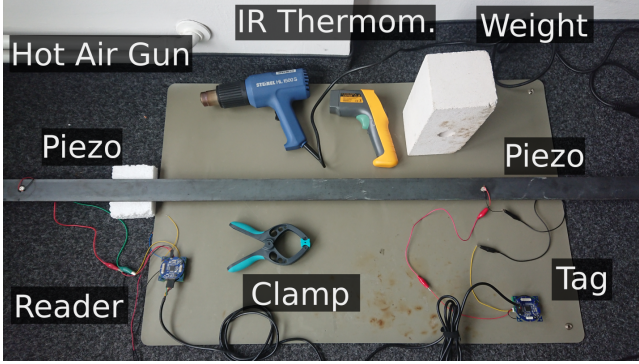


Figure 20. The setup for the dynamic channel experiments, with all used hardware.

provement, especially during the fast heat-up and early cool-down phases, where the channel changes much more rapidly than in the later cool-down phase.

We performed the same experiment in the second scenario, shown in Fig. 19(right). However, instead of heating the metal bar, we applied mechanical forces to it. Forces included clamping the metal locally, putting a 5 kg weight on the metal bar, and stepping on it with full body weight during message transmissions, causing it to bend and change geometry noticeably. In contrast to the first scenario, the channel changes much quicker. Without adaption, the EVM rises to more than three times the initial EVM during transmission, causing high bit error rates. The LMS and CPA algorithms significantly reduced the EVM in response to the changed boundary conditions. Bit errors only occurred in a few messages directly after the change, before the equalizer could adapt. Between LMS and CPA, however, we can not observe further improvement in this scenario.

5.6 IQ Demodulator

The presented analog receiver frontend includes a homodyne demodulator, which is prone to nonlinear distortion of the I and Q parts of the signal. We evaluated the transfer function of our custom demodulator by using two synchronized signal generators to apply two sinusoids with known amplitude and phase offset to the demodulator input while recording the resulting I and Q parts. The demodulated constellation points deviate up to 5% from their expected values in the IQ plane, with an average error of 46 mV.

However, the nonlinearity introduced by the receiver has no significant detrimental effect on the equalizer performance. To quantify the magnitude of the effect, we corrected the recorded samples of 50 messages, using the acquired demodulator transfer function to interpolate samples. When equalizing the corrected samples, the median EVM at the equalizer output was less than 0.2% lower compared to the original recordings. Further improvement of the demodulator circuit's linearity is therefore not highly promising.

6 Limitations and Discussion

The presented results show that software-defined radio techniques such as symbol timing recovery and equalization achieve higher data rates in acoustic backscatter communication and use available bandwidth more efficiently. We

demonstrated this in a highly challenging environment: The guided-wave ultrasonic backscatter channel. A few remarks are appropriate:

The extents of the structure under test were only a 3.5 m long narrow metal bar that was isolated from its environment. In real applications, e.g., in pipeline monitoring, larger structures must be expected, where more wave energy is dissipated into the environment, causing the SNR to shrink. However, SNR is in the current implementation limited, as the received signal is the sum of an environmental reflection and the tag's reflection, which can only be amplified up to the power rails of the reader. An improved design, where the constant offset is first analogously removed before amplification would allow to amplify only the scattered signal before sampling, allowing to reach a much larger SNRs even in large structures.

The two experiments in Section 5.5 show that characteristics in the metal channel are susceptible to physical forces and temperature changes. Adaptive equalization can mitigate slowly changing channels effectively. However, improved adaptation techniques may be required to cope with rapid temperature changes. The used LMS algorithm is known to converge very slowly. More complex but faster-converging algorithms, such as Fast Kalman DFE, may handle substantial temperature variations better and enable the presented technique in more challenging environments. Furthermore, field tests in realistic environments, e.g., bridged or pressurized tanks, must be conducted to measure the extent of channel variation in these scenarios.

To make the tag an entirely passive device, it has to harvest energy from its transducer. In this work, we focused on improving the data rates in communication only and did not implement wireless energy transfer. However, we must expect the harvester to impact the scattered signal as it changes the load impedance at the tag's transducer, e.g., when using switched charge pumps or regulators. At the same time, the chosen load impedance of the transducer can inhibit harvesting if it causes a significant impedance mismatch. Therefore, further research is necessary to combine harvesting and communication in a balanced way.

6.1 Related Work

In this section, we position our contribution in the context of related work, comparing it with the state-of-the-art in acoustic communications and higher-order load modulation.

6.1.1 Acoustic Backscatter Communication

Acoustic backscatter has been applied to several domains, such as underwater, in-body, or through-metal channels. In all of them, data rates are strongly limited by ISI due to the multipath characteristics of acoustic channels. Accordingly, in underwater backscatter [2, 3], bitrates of up to 3 kbit s^{-1} could be achieved, while no equalization was employed.

We explored acoustic backscatter communication in GW metal channels in our previous work in [18], reusing our previous tag design. We extended the reader with an analog IQ demodulator, allowing efficient demodulation at a higher frequency resolution. A significant advancement over our previous work is symbol-timing recovery and equalization. Accordingly, data rates previously did not surpass 1.2 kbit s^{-1}

over 3 m, or 2.5 kbits^{-1} over 1 m, requiring extremely high orders of modulation ($N = 32$). For comparison, we achieved up to 10 kbits^{-1} in the same channels. Similarly, even active communication approaches in GW metal channels did not exceed 7 kbits^{-1} [10], where an MFSK scheme was employed to limit ISI. To the best of our knowledge, all remaining prior work on through-metal backscatter communication related to sandwich plated channels (SWP) over ranges of a few centimeters. SWP channels can employ longitudinal waves as carriers, utilizing much higher bandwidth and less location dependence. The highest reported data rate was achieved in [20] with up to 55 kbits^{-1} without equalization, while ISI was a limiting factor. We have given a comprehensive overview of GW and SWP channels in [18].

6.1.2 Higher-Order Backscatter Modulation

Previous work on through-metal backscatter communication has employed binary modulation, e.g., by switching the transducer between open and closed state. Similarly, only the envelope of the received waveform was acquired at the receiver. Hence, available bandwidth could be used more effectively with higher-order modulation schemes and QAM demodulation. Higher-order backscatter modulation was shown in underwater environments [3] and in RF backscatter [6]. Both works used fixed impedances at the tag to generate different reflection coefficients, yielding a perfect constellation. This suggests that either the input impedance of the transducer was influenced little by the specific channel or that the authors chose the tag's load impedances to match the channel under test. In any case, the distorted constellation was not a challenge. Hence, with known reflection coefficients, [3, 6] employed standard equalization techniques.

7 Conclusion

This work thoroughly investigated the guided-wave metal channel for acoustic backscatter communication. A particular challenge posed by this channel is the strong influence of the channel on a transducer's input impedance, making it impossible to choose the best load impedances to produce the desired constellation before deployment. The resulting distorted constellation is a nonlinear channel, not fit for standard equalization. We presented a channel model where an equivalent linear channel can be constructed, relying only on the steady-state constellation points that the reader can acquire with a pilot sequence. We then evaluated the potential to enhance data rates in the guided-wave metal channel by using an MMSE and a decision feedback equalizer. In a parameter study, we analyzed the required equalizer length, pilot sequence length, and potential improvement of channel coding. We further extended the well-known LMS algorithm for adapting equalizer parameters to a time-varying channel, so that also variations to the distorted constellation can be tracked and tested this adaption technique in real-world scenarios. Finally, we demonstrated that with the described techniques, we increased data rates in the backscatter channel to more than five times the rate achieved without equalization with little additional computational overhead.

8 References

[1] S. S. Afzal, R. Ghaffarivardavagh, W. Akbar, O. Rodriguez, and F. Adib. Enabling Higher-Order Modulation for Underwater Backscat-

ter Communication. In *Global Oceans 2020: Singapore – U.S. Gulf Coast*, pages 1–6, 2020.

[2] R. Bloom, M. Zuniga, Q. Wang, and D. Giustiniano. Tweeting with Sunlight: Encoding Data on Mobile Objects. In *Proceedings of the IEEE INFOCOM 2019*, pages 1324–1332, 2019.

[3] L. Ding, K. Chen, F. Huang, F. Yang, and L. Qian. Modeling and Evaluation of Piezoelectric Transducer (PZT)-Based Through-Metal Energy and Data Transfer. *MDPI Sensors*, 20(11), 2020.

[4] R. Ghaffarivardavagh, S. S. Afzal, O. Rodriguez, and F. Adib. Ultra-Wideband Underwater Backscatter via Piezoelectric Metamaterials. In *Proceedings of the ACM SIGCOMM'20*, page 722–734. ACM, 2020.

[5] M. M. Ghanbari and R. Muller. Optimizing Volumetric Efficiency and Backscatter Communication in Biosensing Ultrasonic Implants. *IEEE Transactions on Biomedical Circuits and Systems*, 14(6):1381–1392, 2020.

[6] A. Goldsmith. *Wireless Communications*. Cambridge university press, 2005.

[7] R. Guida, N. Dave, F. Restuccia, E. Demirors, and T. Melodia. U-Verse: A Miniaturized Platform for End-to-End Closed-Loop Implantable Internet of Medical Things Systems. In *Proceedings of the ACM SenSys'19*, pages 311–323. ACM, 2019.

[8] M. Helmling, S. Scholl, F. Gensheimer, T. Dietz, K. Kraft, S. Ruzika, and N. Wehn. Database of Channel Codes and ML Simulation Results. www.uni-kl.de/channel-codes, 2019.

[9] J. Jang and F. Adib. Underwater Backscatter Networking. In *Proceedings of the ACM SIGCOMM '19*, pages 187–199. ACM, 2019.

[10] M. Jordão, R. Correia, and N. B. Carvalho. Characterisation and implementation of high-order backscatter modulation for iot applications. *IET Microwaves, Antennas & Propagation*, 13(15):2636–2640, 2019.

[11] M. Kiziroglou, D. Boyle, S. Wright, and E. Yeatman. Acoustic power delivery to pipeline monitoring wireless sensors. *Ultrasonics*, 77:54–60, 2017.

[12] R. Lammering, U. Gabbert, M. Sinapius, T. Schuster, and P. Wierach. *Lamb-Wave Based Structural Health Monitoring in Polymer Composites*. Springer, 2017.

[13] L. Lanbo, Z. Shengli, and C. Jun-Hong. Prospects and problems of wireless communication for underwater sensor networks. *Wireless Communications and Mobile Computing*, 8(8):977–994, 2008.

[14] M. Lunglmayr and M. Huemer. Least squares equalization for rfid. In *2010 Second International Workshop on Near Field Communication*, pages 90–94, 2010.

[15] P. Oppermann and C. Renner. Higher-Order Modulation for Acoustic Backscatter Communication in Metal. In *Proceedings of the ACM SIGCOMM '22*. ACM, 2022.

[16] M. G. L. Roes, J. L. Duarte, M. A. M. Hendrix, and E. A. Lomonova. Acoustic Energy Transfer: A Review. *IEEE Transactions on Industrial Electronics*, 60(1):242–248, 2013.

[17] D. A. Shoudy, G. J. Saulnier, H. A. Scarton, P. K. Das, S. Roa-Prada, J. D. Ashdown, and A. J. Gavens. P3f-5 An Ultrasonic Through-Wall Communication System with Power Harvesting. In *2007 IEEE Ultrasonics Symposium Proceedings*, pages 1848–1853, 2007.

[18] H. Song, H. J. Lim, and H. Sohn. Electromechanical impedance measurement from large structures using a dual piezoelectric transducer. *Journal of Sound and Vibration*, 332(25):6580–6595, 2013.

[19] S. J. Thomas. *Modulated Backscatter for Low-Power High-Bandwidth Communication*. PhD thesis, Duke University, 2013.

[20] S. J. Thomas and M. S. Reynolds. A 96 mbit/sec, 15.5 pJ/bit 16-qam modulator for uhf backscatter communication. In *2012 IEEE International Conference on RFID*, pages 185–190, 2012.

[21] V. F.-G. Tseng, S. S. Bedair, J. J. Radice, T. E. Drummond, and N. Lazarus. Ultrasonic Lamb Waves for Wireless Power Transfer. *IEEE Transactions on Ultrasonics, Ferroelectrics, and Frequency Control*, 67(3):664–670, 2020.

[22] S. Yang and A. C. Singer. Energy Efficient Ultrasonic Communication on Steel Pipes. In *2016 IEEE International Workshop on Signal Processing Systems (SiPS)*, pages 297–302, 2016.